

# Spin State Disproportionation in Insulating Ferromagnetic LaCoO<sub>3</sub> Epitaxial Thin Films

Shanquan Chen, Jhong-Yi Chang, Qinghua Zhang, Qiuyue Li, Ting Lin, Fanqi Meng, Haoliang Huang, Yangyang Si, Shengwei Zeng, Xinmao Yin, My Ngoc Duong, Yalin Lu, Lang Chen, Er-Jia Guo, Hanghui Chen, Chun-Fu Chang, Chang-Yang Kuo,\* and Zuhuang Chen\*

The origin of insulating ferromagnetism in epitaxial LaCoO<sub>3</sub> films under tensile strain remains elusive despite extensive research efforts are devoted. Surprisingly, the spin state of its Co ions, the main parameter of its ferromagnetism, is still to be determined. Here, the spin state in epitaxial LaCoO<sub>3</sub> thin films is systematically investigated to clarify the mechanism of strain-induced ferromagnetism using element-specific X-ray absorption spectroscopy and dichroism. Combining with the configuration interaction cluster calculations, it is unambiguously demonstrated that Co<sup>3+</sup> in LaCoO<sub>3</sub> films under compressive strain (on LaAlO<sub>3</sub> substrate) is practically a low-spin state, whereas Co<sup>3+</sup> in LaCoO<sub>3</sub> films under tensile strain (on SrTiO<sub>3</sub> substrate) have mixed high-spin and low-spin states with a ratio close to 1:3. From the identification of this spin state ratio, it is inferred that the dark strips observed by high-resolution scanning transmission electron microscopy indicate the position of Co<sup>3+</sup> high-spin state, i.e., an observation of a spin state disproportionation in tensile-strained LaCoO<sub>3</sub> films. This consequently explains the nature of ferromagnetism in LaCoO<sub>3</sub> films. The study highlights the importance of spin state degrees of freedom, along with thin-film strain engineering, in creating new physical properties that do not exist in bulk materials.

## 1. Introduction

Perovskite oxides exhibit a variety of electronic properties, including high-temperature superconductivity, colossal magnetoresistance, and multiferroism, as a consequence of complex interplay among lattice, charge, spin, and orbital degrees of freedom.<sup>[1-6]</sup> Epitaxial strain can dramatically alter the physical properties of the strongly correlated oxide materials.<sup>[7]</sup> One notable example is the tensile-strain-induced ferromagnetism in LaCoO<sub>3</sub> (LCO) epitaxial thin films.<sup>[8-10]</sup> Bulk LCO is a diamagnetic insulator below  $\approx 100$  K due to a low-spin (LS,  $t_{2g}^6 e_g^0$ ,  $S = 0$ ) ground-state configuration of Co<sup>3+</sup>, and becomes paramagnetic at higher temperature with the increasing population of Co<sup>3+</sup> high-spin (HS,  $t_{2g}^4 e_g^2$ ,  $S = 2$ ) state.<sup>[11]</sup> Although this intriguing system has been studied extensively for decades,<sup>[9,12-17]</sup> the origin of insulating ferromagnetism in tensile-strained LCO films still remains

S. Chen, Y. Si, Z. Chen  
School of Materials Science and Engineering  
Harbin Institute of Technology  
Shenzhen 518055, China  
E-mail: zuhuang@hit.edu.cn


J.-Y. Chang, M. N. Duong, C.-Y. Kuo  
Department of Electrophysics  
National Yang Ming Chiao Tung University  
Hsinchu 30010, Taiwan  
E-mail: changyangkuo@nycu.edu.tw

Q. Zhang, T. Lin, F. Meng, E.-J. Guo  
Beijing National Laboratory for Condensed Matter Physics and Institute  
of Physics  
Chinese Academy of Sciences  
Beijing 100190, China

Q. Li  
Department of Electronic Science  
East China Normal University  
Shanghai 200241, China

Q. Li, H. Chen  
NYU-ECNU Institute of Physics  
NYU Shanghai  
Shanghai 200124, China

H. Huang, Y. Lu  
Hefei National Research Center for Physical Sciences at the Microscale  
and Anhui Laboratory of Advanced Photon Science and Technology  
University of Science and Technology of China  
Hefei 230026, China

 The ORCID identification number(s) for the author(s) of this article can be found under <https://doi.org/10.1002/advs.202303630>

© 2023 The Authors. Advanced Science published by Wiley-VCH GmbH. This is an open access article under the terms of the Creative Commons Attribution License, which permits use, distribution and reproduction in any medium, provided the original work is properly cited.

DOI: 10.1002/advs.202303630

controversial. Previous investigations have proposed several competing models for the mechanism governing the ferromagnetism in the LCO films,<sup>[12–15,18–24]</sup> including orbital order composed of Co<sup>3+</sup> intermediate spin (IS,  $t_{2g}^5 e_g^1$ ,  $S = 1$ ) and/or Co<sup>3+</sup> HS state,<sup>[13,18]</sup> superexchange-like interaction between LS Co<sup>3+</sup> and HS Co<sup>2+</sup> induced by oxygen vacancies,<sup>[14–15]</sup> spin-state order among Co<sup>3+</sup> LS and HS<sup>[12,19]</sup> or IS state,<sup>[20]</sup> charge order/disproportionation,<sup>[21–22]</sup> intrinsic twin domains with HS/IS and LS state order, etc.<sup>[22–23]</sup> Apparently, the spin state of Co ions in strained LCO films is a key factor for its ferromagnetism. Yet, its spin states are controversially reported.

Here, to understand the nature of insulating ferromagnetism in epitaxial LCO films, we have engaged a systematic study using soft X-ray absorption spectroscopy (XAS), X-ray linear dichroism (XLD) spectroscopy, magnetic circular dichroism (XMCD) spectroscopy and high-resolution scanning transmission electron microscopy (STEM). Combining with the configuration cluster-interaction (CI) calculations, we reveal that the Co<sup>3+</sup> ions in films under tensile strain (on SrTiO<sub>3</sub>, STO) consist of both the LS and HS states and, importantly the ratio of HS to LS in cobalt ions is  $\approx 1:3$ , whereas the Co<sup>3+</sup> ions in films under compressive strain (on LaAlO<sub>3</sub>, LAO) possess mainly an LS state. This HS to LS ratio of 1:3 naturally explains the low net magnetic moment of  $1 \mu_B/\text{Co}$  in the tensile strained films. Microscopically, we investigated the origin of the commonly observed stripe patterns in STEM images with different electron dose conditions. With a high electron dose, we observed a dark- to bright-strip ratio of  $\approx 1:3$  in the tensile strained LCO/STO films, whereas with a low electron dose a homogeneously bright image was observed. The images from the LCO/LAO films are electron dose-independent and have no dark stripes. This indicates that the dark stripes could be the area of HS state, but the formation of the dark stripes due to oxygen va-

cancies ordering is extrinsic. Important is that there is an intrinsic HS- and LS-state disproportionation in the LCO/STO films. This Co<sup>3+</sup> HS and LS disproportionation provides a particular ferromagnetic coupling of the Co<sup>3+</sup> HS intermediated by the Co<sup>3+</sup> LS for the ferromagnetism in the tensile strained films.

## 2. Results and Discussion

High-quality LCO films with a thickness of 12 nm were grown on [001]-oriented STO and LAO substrates by pulsed laser deposition (see details in Experimental Section). All LCO films have smooth surfaces and are coherently strained to the underlying substrates (Figure 1; Figure S2, Supporting Information). Only (00 $l$ ) diffraction peaks from the films and substrates are visible, indicating that the LCO films are free of impurities (Figure 1a). XRD phi scans indicate the cube-on-cube epitaxy growth of the films on the substrates (Figure S3, Supporting Information). Combined with the results of the X-ray reciprocal-space mappings (RSM) along the pseudocubic (013) direction (Figure 1b,c), the out-of-plane lattice parameter of the LCO films shrink (expand) when the films are epitaxially grown on tensile-STO (compressive-LAO) substrates because of the Poisson effect. Furthermore, the Phi- angles-dependent RSMs and rocking curves show the existence of satellite peaks (Figures S4 and S5, Supporting Information), indicating a periodic in-plane nanodomain modulation (Figure S6, Supporting Information). Figure 1d displays the SQUID magnetometry results for the films. Similar to bulk LCO, the film grown on LAO does not show any discernible ferromagnetic transition or hysteresis loop (Figure 1d). In contrast, LCO grown on STO shows a distinct magnetic transition at 80 K and a clear ferromagnetic hysteresis loop with saturation magnetization of  $\approx 1 \mu_B/\text{Co}$  at 10 K, indicates a ferromagnetic order with  $T_C \approx 80$  K. Furthermore, the transport measurement reveals that the LaCoO<sub>3</sub> films show insulating behavior (Figure 1e). The macroscopic magnetic and transport measurement results are consistent with previous studies.<sup>[9,15,22,25–27]</sup>

To figure out the spin states in LCO films, we measured the XAS at Co  $L_{2,3}$  edges. The XAS at the  $L$  edges measure the excitations of electrons from the  $2p$  core levels to the  $3d$  unoccupied states. The strong Coulomb interaction between a  $2p$  core-hole and  $3d$  electrons narrows the  $3d$  bandwidth and enhances the local solid-state effect. It makes the XAS a suitable tool to investigate the local spin state and orbital occupation.<sup>[10,28–30]</sup> Figure 2a shows the experimental Co  $L_{2,3}$  XAS spectra taken from LCO films grown on STO and LAO substrates at 30 K. Obviously, Co<sup>3+</sup> is the main valence state of Co ion in both films. Besides, clear spectral differences between the XAS spectrum of LCO/STO and LCO/LAO are observed (Figure 2b). It is important to note that the XAS difference shown in Figure 2 for LCO between the two different strain states is similar to previous results on bulk LCO measured at high and low temperatures, respectively.<sup>[10]</sup> It indicates a spin-state difference of Co ions for LCO films under compressive strain and tensile strain.

To look for insight into XAS, we simulate the XAS spectra of Co<sup>3+</sup> ions with different spin states by employing the CI cluster calculations with full atomic multiplet theory. We first calculated the XAS spectra for Co<sup>3+</sup> ions in pure LS and pure HS states (Figure 2a). One can see that the calculated XAS spectra for pure HS and LS states nicely reproduce the experimental XAS of

S. Zeng  
Department of Physics  
Faculty of Science  
National University of Singapore  
Singapore 117551, Singapore

X. Yin  
Shanghai Key Laboratory of High Temperature Superconductors  
Physics Department  
Shanghai University  
Shanghai 200444, China

L. Chen  
Department of Physics  
Southern University of Science and Technology  
Shenzhen 518055, China

H. Chen  
Department of Physics  
New York University  
New York, NY 10012, USA

C.-F. Chang  
Max-Planck Institute for Chemical Physics of Solids  
Nöthnitzer Str. 40, 01187 Dresden, Germany

C.-Y. Kuo  
National Synchrotron Radiation Research Center  
101 Hsin-Ann Road, Hsinchu 30076, Taiwan

Z. Chen  
Flexible Printed Electronics Technology Center  
Harbin Institute of Technology  
Shenzhen 518055, China

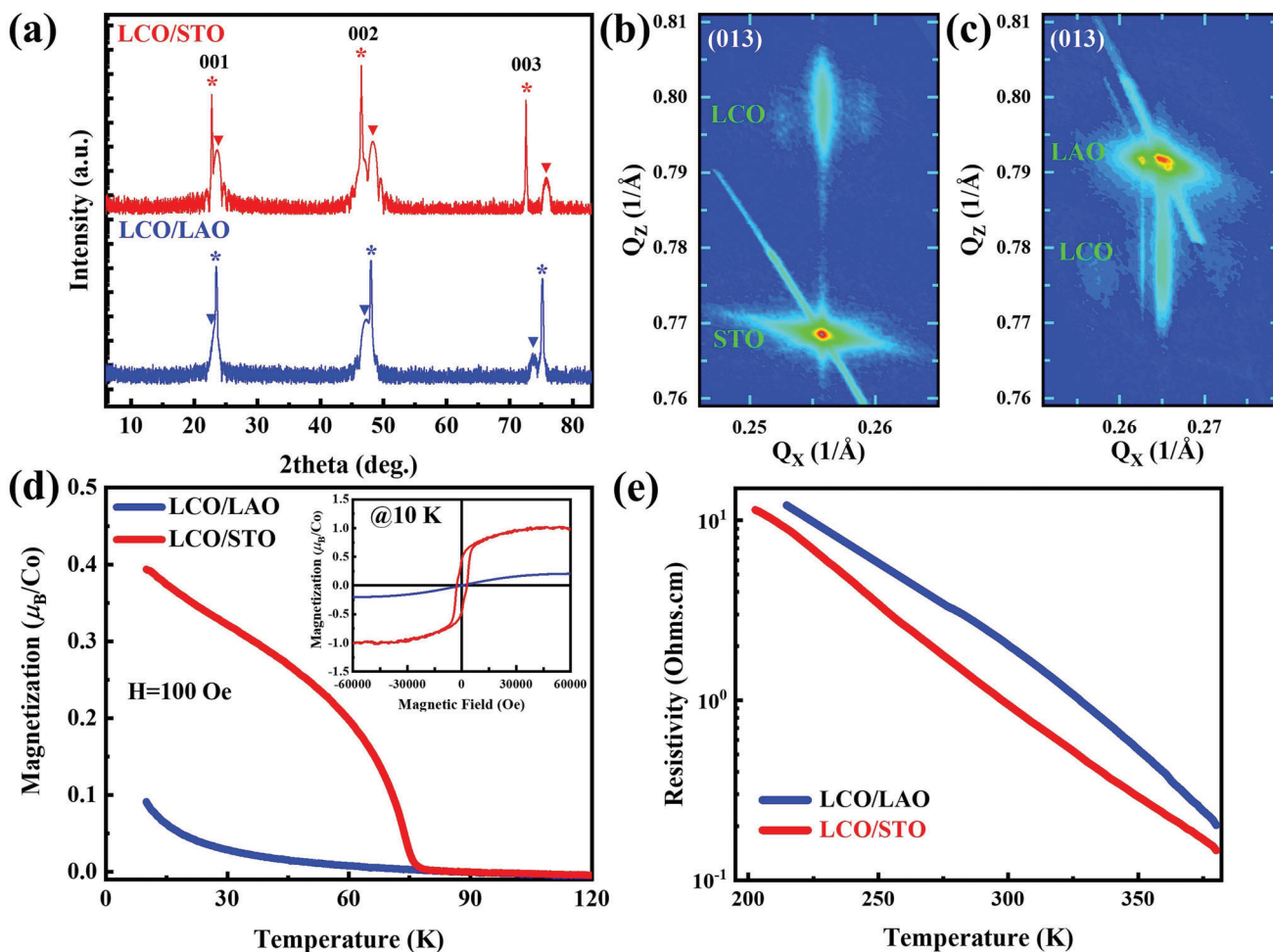


**Figure 1.** Structural, magnetic, and electrical transport properties of LCO films grown on STO and LAO substrates. a) X-ray diffraction  $2\theta$ - $\omega$  scan around the 001 and 002 reflections of LCO films grown on STO and LAO substrates. The peaks of substrates and LCO films are indicated with asterisk “\*” and inverted triangle “▼”, respectively. b,c) Reciprocal space mappings (RSM) of LCO films grown on STO and LAO around the substrate’s (013) reflection, respectively. d) Magnetization–temperature ( $M$ – $T$ ) curves and magnetic hysteresis ( $M$ – $H$ ) loops measured at 10 K (the inset) of LCO films grown on  $\text{LaAlO}_3$  (001) and  $\text{SrTiO}_3$  (001) substrates. The  $M$ – $T$  curves were measured at the magnetic field of 100 Oe applied along the film plane. e) Temperature-dependent resistivity measured under zero magnetic field for 12 nm  $\text{LaCoO}_3$  films grown on  $\text{LaAlO}_3$  (001) and  $\text{SrTiO}_3$  (001) substrate, respectively.

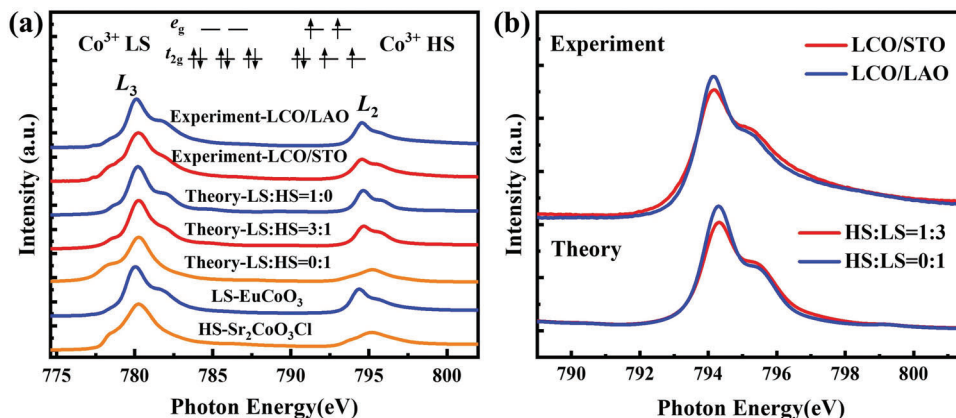


**Figure 2.** a) Experimental  $\text{Co } L_{2,3}$  XAS spectra taken from LCO films grown on LAO and STO substrates at 30 K, together with the theoretical XAS spectra in the LS-HS scenario and reference spectra for LS  $\text{Co}^{3+}$  ( $\text{EuCoO}_3$ ) and HS  $\text{Co}^{3+}$  ( $\text{Sr}_2\text{CoO}_3\text{Cl}$ ). b) The experimental  $\text{Co } L_2$  XAS spectra of LCO/LAO and LCO/STO at 30 K and the corresponding theoretical isotropic spectra in the LS-HS scenario.

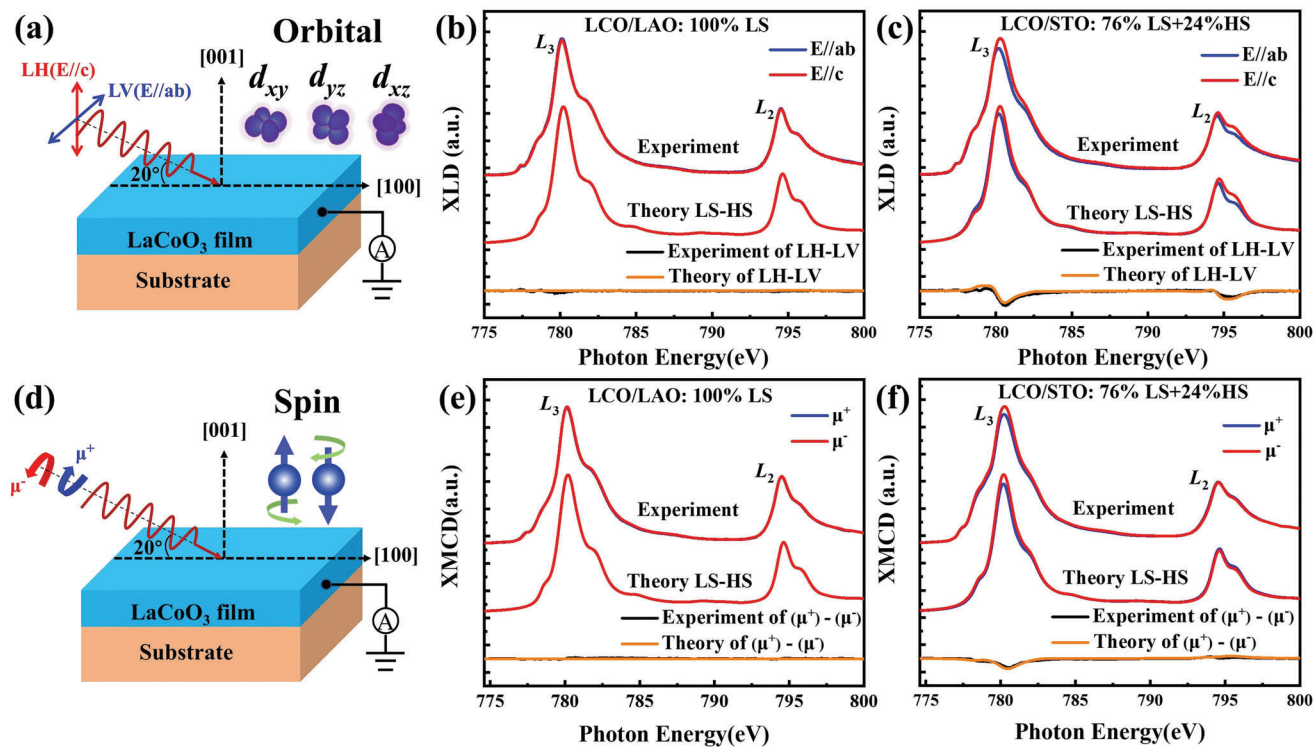


**Figure 3.** Left panels: A sketch of the a) XLD and d) XMCD measurements. The XLD was obtained from the difference for XAS measured with linear horizontal and linear vertical polarized light. The XMCD was obtained from the difference for XAS measured with left ( $\mu^+$ ) and right ( $\mu^-$ ) circularly polarized light. Before the XMCD measurement, the LCO films are first magnetized by a magnetic field of 1 Tesla. In Both XLD and XMCD measurements, the X-ray beam was incident on the sample at an angle of  $20^\circ$  from the sample surface. Right panels: Top: Experimental Co  $L_{2,3}$  XAS spectra and XLD at 30 K for b) LCO/LAO and c) LCO/STO, together with the corresponding theoretical XAS and XLD spectra calculated in the LS-HS scenario. Bottom: Experimental Co  $L_{2,3}$  XAS spectra and XMCD at 30 K for e) LCO/LAO and f) LCO/STO using circularly polarized X-rays, together with the theoretical XAS and XMCD spectra for LCO/LAO and LCO/STO calculated in the LS-HS scenario.

$\text{Sr}_2\text{CoO}_3\text{Cl}$  and  $\text{EuCoO}_3$  (Figure 2a), in which the former compound has  $\text{Co}^{3+}$  ions in a pure HS state but the latter in a pure LS state.<sup>[28–30]</sup> We next did the linear combination of HS and LS XAS spectra to fit the experimental XAS spectra of LCO films. The curves in Figure 2b show the experimental XAS spectra and theory spectra calculated with a pure LS state (blue) and with HS:LS $\approx$ 1:3 mixed spin states (red). One can see that the theoretical spectra are in good agreement with the experimental ones. Other cases with different ratios of HS/LS states were also included by CI calculations, but the HS:LS = 1:3 calculated by CI best fits the experimental result (Figure S7, Supporting Information). The results indicate that  $\text{Co}^{3+}$  in LCO/LAO contains mainly an LS state, while  $\text{Co}^{3+}$  in LCO/STO is a mixed spin state with an HS to LS ratio of 1:3.

To further confirm the  $\text{Co}^{3+}$  spin state in the LCO films, we measured the XLD spectra in grazing incidence geometry (Figure 3a). In principle, the XLD originates from two contributions, namely the orbital anisotropy and the magnetic contribution. The XLD spectra shown in Figure 3 were collected after LCO cooling down from room temperature to  $T = 30$  K without applying a magnetic field. One can thus expect no long-range magnetic order presenting in LCO and the contribution from magnetism to XLD is minimal. That is, the orbital anisotropy should be the main origin for causing the XLD signal. Under the LS state, six electrons fully occupy six  $t_{2g}$  orbitals, making the ground state

wavefunction nearly spherical symmetry. There is thus no orbital anisotropy and the XLD is expected to be rather small for  $\text{Co}^{3+}$ -ion under the LS state. In Figure 3b, one sees that the XLD signal of  $\text{Co}^{3+}$ -ion in the compressive LCO film is negligibly small, indicating essentially no orbital anisotropy for the LS state. The XAS spectra calculated for  $E//c$  and  $E//ab$  shown in Figure 3b under a pure LS state generate no XLD signal, which reproduces the experimental results and reveals the nearly 100% LS state for  $\text{Co}^{3+}$ -ion in the compressive LCO/LAO film.

In contrast, as shown in Figure 3c, the tensile-strained LCO/STO film exhibits clear linear dichroism. For an HS state of  $\text{Co}^{3+}$ -ion, five majority spin electrons, half-filling the  $3d$  orbitals, make a spherical symmetry of wavefunction, and a minority spin electron occupying a specific orbital can cause an orbital anisotropy and give rise to XLD signals for the film. The XLD signal in Figure 3c clearly shows that the intensity of XAS for  $E//c$  is stronger than that of  $E//ab$ . This indicates that a portion of  $\text{Co}^{3+}$  cations is an HS state in the tensile-strained LCO film, and the orbital occupied by the minority spin electron of the  $\text{Co}^{3+}$  ions is in the  $ab$ -plane of the film. To address the HS contribution to XLD, we calculated the XAS spectra of HS  $\text{Co}^{3+}$  ions by considering the energy of  $d_{xy}$  orbital lower than that of  $d_{xz}/d_{yz}$  by  $\approx 50$  meV. A minority spin electron of HS  $\text{Co}^{3+}$  ions thus occupies the  $d_{xy}$  orbital and causes the orbital anisotropy, which fully accords to the tensile-strain status of the LCO/STO film. To simulate the



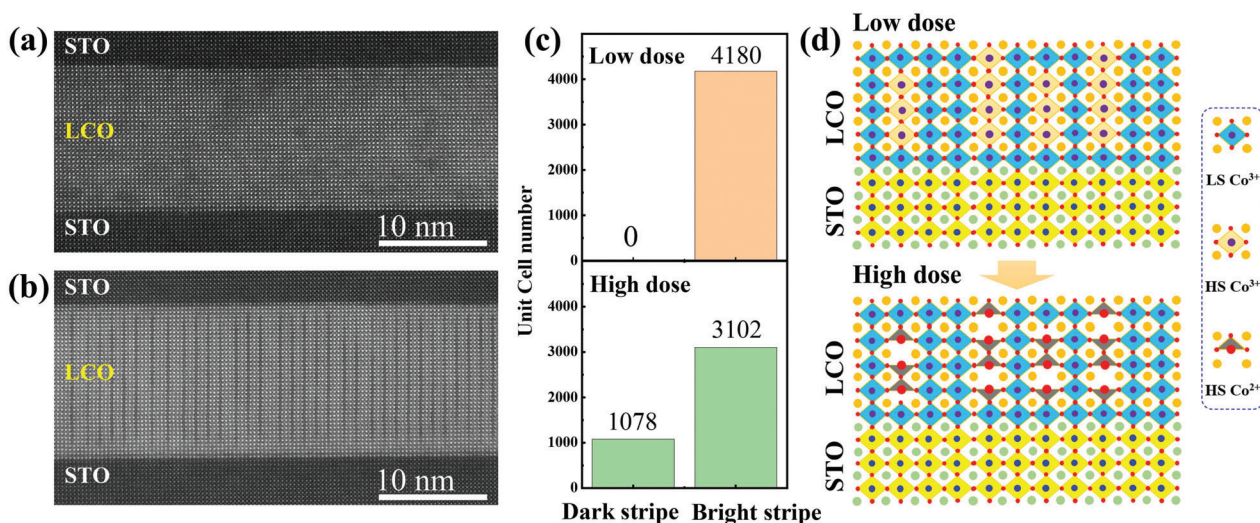


**Figure 4.** High-resolution HAADF STEM image of a LCO film grown on an STO substrate with an STO capping layer on top with different electron dose condition; a) low- and b) high-dose conditions. c) Unit cell number containing dark and bright stripe at low and high dose conditions, respectively. d) The schematic diagram of the  $\text{LaCoO}_3/\text{SrTiO}_3$  (001) under low electron dose condition and  $\text{LaCo}_{3-\delta}/\text{SrTiO}_3$  (001) under high electron dose condition. The dotted box on the right side of the schematic denotes the unit cell with LS  $\text{Co}^{3+}$ , HS  $\text{Co}^{3+}$ , and HS  $\text{Co}^{2+}$ , respectively. The yellow substrate represents  $\text{SrTiO}_3$  (001).

experimental XLD spectrum of LCO/STO, we have carried out a simple simulation by making a superposition of the calculated HS and LS XLD spectra. We found that the spectra with an HS to LS ratio of 1:3 reproduce the experimental spectra the best as shown in Figure 3c, which is consistent with the ratio obtained for simulating the isotropic XAS spectrum. Another piece of important information is that this occupied  $d_{xy}$  orbital of HS  $\text{Co}^{3+}$  may explain the in-plane magnetic easy axis in LCO/STO films.<sup>[31]</sup>

The presence of  $\text{Co}^{3+}$  HS in LCO/STO films offers the essential for its ferromagnetism. To clarify the contribution of  $\text{Co}^{3+}$  HS state to ferromagnetism, we carried out remanent XMCD experiments on magnetized LCO/LAO and LCO/STO at  $T = 30$  K (Figure 3d). Figure 3e,f shows experimental XAS spectra taken with circularly polarized light on the LCO films. The XMCD measurement demonstrates a consistent result with the above macroscopic magnetic properties measured in magnetometry. Spectra of LCO/LAO (Figure 3e) show an almost zero dichroism signal, indicating no spontaneous magnetization. Spectra of LCO/STO (Figure 3f) exhibit a clear dichroism signal, addressing a net ferromagnetic order of the  $\text{Co}^{3+}$  ions at 30 K. To address the origin of the XMCD, we again simulate the XMCD spectra by CI cluster calculations. We take the same ratio of two spin states found by both the XAS and XLD simulations, a pure LS state for LCO/LAO film and HS:LS = 1:3 for LCO/STO film, to calculate the XMCD spectra. The results are also included in Figure 3. It is not surprising to see that the calculated XMCD for LCO/LAO is zero because of a pure LS ( $S = 0$ ) state. The calculation for LCO/STO with HS:LS = 1:3 exhibits a clear XMCD signal and the calculated spectra nicely reproduce the experimental spectra. Hence, it is the HS  $\text{Co}^{3+}$ -ions that contribute to the XMCD signal and form the ferromagnetic order. It is worthwhile to mention that this HS to LS ratio of 1:3 naturally explains the low net magnetic moment of  $\approx 1 \mu_B/\text{Co}$  in the LCO/STO films from the above SQUID magnetometry results. We also use first-principles cal-

culations to study the LS state of LCO under LAO substrate and a mixed-spin state (HS:LS = 1:3) of LCO under STO substrate. In both spin configurations, an insulating state is found in the calculations. In the mixed-spin state, calculations also find a net magnetization of  $\approx 1 \mu_B$  per formula (Figure S8, Supporting Information).

So far, using high-resolution STEM lattice modulations in the form of atomic-scale stripe patterns were commonly observed.<sup>[14–15,22–23,27,32–34]</sup> However, not only the origin of the dark stripes observed in LCO/STO has been debated,<sup>[14,22–23,27,32–33]</sup> but also various spin state models were proposed.<sup>[14,23,32]</sup> To clarify the relationship between the microstructure and the  $\text{Co}^{3+}$  spin state, we performed high-resolution STEM measurements on LCO/LAO and LCO/STO films (Figure 4; Figure S9, Supporting Information). We paid special attention to the used electron dose, since the STEM technique is not a non-destructive technique, a high-energy electron beam could damage/reduce the LCO thin films to a certain extent, resulting in a change in its stoichiometry.<sup>[35]</sup> Figure 4 shows the high-angle annular dark-field (HAADF) STEM images of different stages of the beam exposure experiment on LCO/STO. Under low-dose electron beam irradiation ( $\approx 10^6 \text{ e}^-/\text{angstrom}^2$ ), no dark stripes are seen in the STEM image (Figure 4a). However, as the electron beam irradiation dose increases ( $\approx 10^8 \text{ e}^-/\text{angstrom}^2$ ), we observed clearly ordered dark stripes in the STEM image (Figure 4b). According to statistics, the ratio of the unit cells where the dark and bright stripes are located is  $\approx 1:3$  (Figure 4c). In contrast, no dark stripes were observed in STEM images for compressive LCO film grown on LAO under both low-dose and high-dose electron beam irradiation conditions (same irradiation as LCO/STO) (Figure S9, Supporting Information). These results are consistent with previous literature reports.<sup>[14–15,22–23]</sup> Although the exact origin of dark stripes cannot be directly determined by STEM, however, this invites a comparison with the HS–LS ratio of 1:3 found by

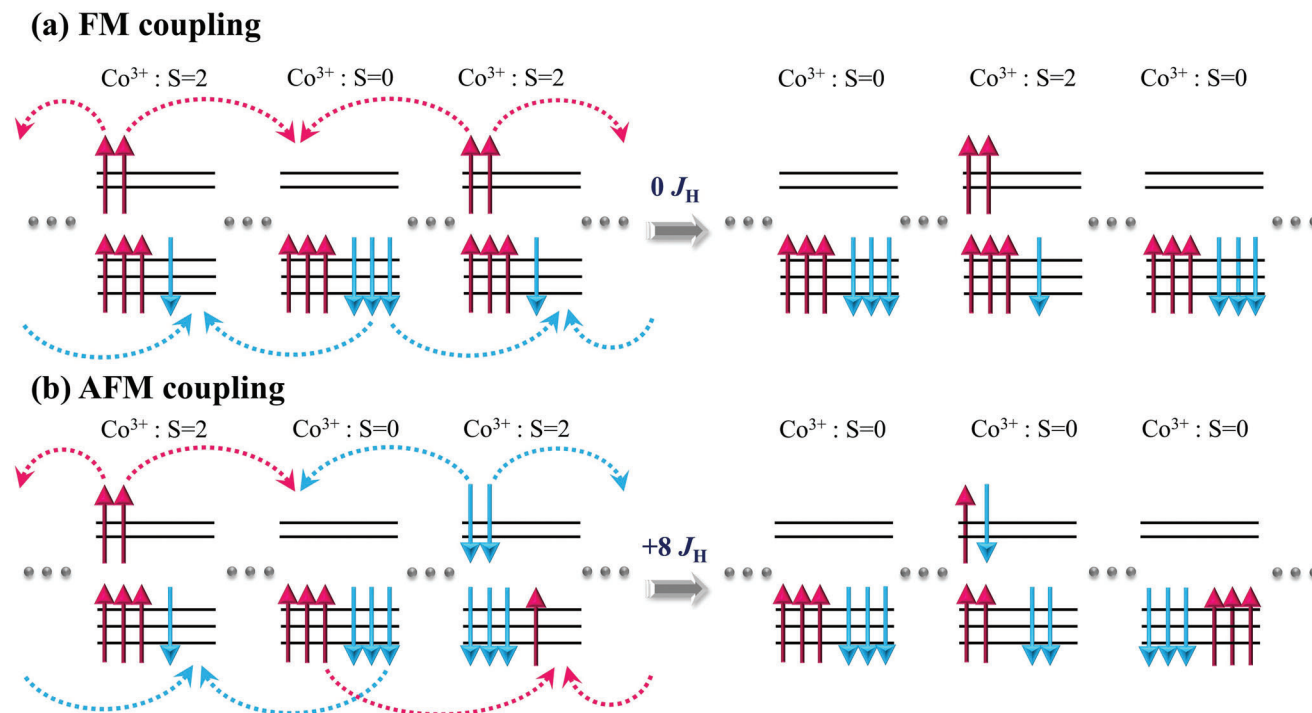


**Figure 5.** The schematic diagram of the magnetic interactions between HS and LS  $\text{Co}^{3+}$  ions with a) ferromagnetic and b) antiferromagnetic coupling. Its virtual hopping processes are as follows. The two  $e_g$  electrons of an HS  $\text{Co}^{3+}$  site hop evenly left and right to the neighboring LS  $\text{Co}^{3+}$  sites. Two of the six  $t_{2g}$  electrons of each LS  $\text{Co}^{3+}$  site do a similar hopping but among  $t_{2g}$  orbitals. This virtual hopping process prefers a ferromagnetic coupling because an antiferromagnetic coupling will lead to a wrong spin state configuration with an additional energy cost of  $8J_H$  with respect to a ferromagnetic coupling. The blue dots represent LS  $\text{Co}^{3+}$  sites. The number of the LS  $\text{Co}^{3+}$  intermediate between the HS  $\text{Co}^{3+}$  sites can be altered.

the above-mentioned XAS results. It is reasonable to speculate that the position of the dark stripes is not random, but maybe the place where the high-spin state  $\text{Co}^{3+}$  is (Figure 4d). We have further verified this assignment by using electron-energy-loss spectroscopy (EELS) (Figure S11, Supporting Information). For LCO/LAO, there is no difference in the shape, intensity, and peak position of the O-K and Co-L edges of bright stripes in different regions. However, the clear differences between the EELS in the dark (blue line) and bright stripes (red line) in the LCO/STO film are seen. The front peak (light golden area) intensity of the O-K edge corresponding to the dark stripes is lower than that of the bright stripes pattern, which indicates the formation of oxygen vacancies along these places. In addition, the dark stripes have a higher  $L_3/L_2$  peak intensity ratio than the bright stripes at the Co-L edges. These findings indicate that the oxidation state of Co along the dark stripes has been reduced by a relatively high dose of electron beam. It is well-known that the metal ion-ligand bond of HS is weaker than that of LS, therefore, the oxygen ions around the HS are likely to be knocked out more easily.<sup>[36–39]</sup> This HS-dark stripe and LS-bright stripe assignment are also supported by the bond-length modulation observation by STEM studies as the ionic radius of HS  $\text{Co}^{3+}$  is larger than that of LS  $\text{Co}^{3+}$ .<sup>[32]</sup> We conclude that the commonly observed dark stripes in LCO/STO films are an extrinsic reduction of oxygen by a high-dose electron beam used in STEM. Yet, most importantly, it gives access of a direct atomic-scale positioning of HS  $\text{Co}^{3+}$  ions, evidencing an intrinsic HS and LS disproportionation in LCO/STO films.

We in fact restore the HS and LS disproportionated insulating phase for bulk LCO at intermediate temperature.<sup>[40]</sup> The advance of LCO/STO film is that by strain engineering, this HS and LS disproportionation is realized at low temperature or as the ground state. The spin state of the  $\text{Co}^{3+}$  ions in LCO is mainly determined by the competition between the crystal-field splitting  $\Delta_{CF}$  and the Hund's exchange interaction  $J_H$ .<sup>[10]</sup> The crystal field splitting results from the Co-ligand interaction, which splits the five degenerate  $3d$  orbitals of the Co-ion into two groups,  $e_g$  and  $t_{2g}$ , with the energy of  $t_{2g}$  lower than that of  $e_g$ . The magnitude of the crystal field splitting is determined by the Co–O bond length. The smaller the Co–O bond length, the larger the crystal field splitting. Therefore, the crystal field splitting favors six electrons of  $\text{Co}^{3+}$  to fill the  $t_{2g}$  orbital, forming the LS state. However, the LS state violates Hund's rule, which makes it unstable with respect to the Coulomb repulsion energy. The Co–O bond length, extended by any disturbances such as thermal expansion, would suppress the crystal field splitting and induce the HS state to stabilize the Coulomb repulsion energy. Therefore, the pure LS spin state of LCO is observed only at low temperatures.<sup>[10]</sup> The LCO film in this work under tensile strain has an average Co–O bond length longer than that of one under compressive strain.<sup>[41]</sup> Apparently, the tensile strain enforced by STO is on the border of LS and HS formation.<sup>[19]</sup> The longer Co–O bond length would weaken the crystal field splitting, causing the system to select some region in the film to stabilize in a state following Hund's rule to form the HS state. This explains the appearance of the HS state in the tensile LCO film.

The HS and LS state disproportion in LCO/STO plays an important role in its magnetism.<sup>[12,19]</sup> Figure 5 displays a sketch of the superexchange-like process of  $t_{2g}$  and  $e_g$  electrons in an HS–LS–HS configuration for both ferromagnetic and antiferromagnetic couplings. In the ferromagnetic coupling model, the two  $e_g$  electrons of an HS  $\text{Co}^{3+}$  site jump equally left and right to the neighboring LS  $\text{Co}^{3+}$  sites. Two of the six  $t_{2g}$  electrons of each LS  $\text{Co}^{3+}$  site perform a similar hopping but between  $t_{2g}$  orbitals. The mutual jumping of the electrons results in no net charge transfer and ends up in the same spin state configuration as the initial state (Figure 5a). In contrast, the antiferromagnetic coupling brings the system to a different spin state configuration (Figure 5b). It is clear to see that the ferromagnetic coupling is energetically more favorable than the antiferromagnetic coupling by  $8J_H$ . Thus, the system prefers the ferromagnetic coupling as the ground state. We note that this energetic superiority of the ferromagnetic coupling of  $\text{Co}^{3+}$  ions also holds for configurations such as HS–LS–LS–HS and HS–LS–LS–LS–HS and so on, once the  $\text{Co}^{3+}$  HS is mediated by the LS. The event of each electron jumps costs the energy of the Coulomb repulsion. Thus, the system remains as an insulating state under ferromagnetic coupling. The insulating ground state of tensile strain LCO film was further supported by our DFT calculations (Figure S8, Supporting Information).

### 3. Conclusion

In summary, using a combination of element-specific X-ray absorption spectroscopy and dichroism together with the configuration interaction cluster calculations, we unambiguously demonstrate that Co ions in LCO/LAO thin films under compressive strain are practically a low-spin state, whereas Co ions in LCO/STO thin films under tensile strain have mixed high-spin and low-spin states with a ratio close to 1:3. From the identification of this spin state ratio, we infer that the dark strips in LCO/STO observed by STEM indicate the position of  $\text{Co}^{3+}$  high-spin state. Yet, these dark strips are extrinsically caused by the high dose of electron beam used in STEM. Most importantly, this provides access to experimentally observe the  $\text{Co}^{3+}$  HS and  $\text{Co}^{3+}$  LS state disproportionation in LCO/STO. In such an HS and LS state disproportionation, the ferromagnetic coupling of the  $\text{Co}^{3+}$  HS intermediated by  $\text{Co}^{3+}$  LS is energetically more favorable than the antiferromagnetic coupling.

### 4. Experimental Section

**LaCoO<sub>3</sub>(LCO) Films Growth and Structural Characterization:** High quality LCO films ( $\approx 12$  nm) were grown on [001]-oriented single crystal SrTiO<sub>3</sub> (STO) and LaAlO<sub>3</sub> (LAO) substrates by pulsed laser deposition (Arrayed Materials RP-B). During the film deposition, the KrF excimer laser ( $\lambda = 248$  nm) energy density and ablation repetition were given 1.5 J cm<sup>-2</sup> and 3 Hz, respectively. The deposition temperature was kept at 700 °C, and the oxygen pressures during film deposition was maintained at 20 Pa. All films were cooled down (10°C min<sup>-1</sup>) to room temperature with 10 000 Pa of oxygen atmosphere to ensure the oxygen stoichiometry. High-resolution X-ray diffraction (XRD) measurements were performed on a Rigaku-Smartlab, 9 KW diffractometer with Cu K<sub>α1</sub> radiation. The morphology was determined by an Asylum Research MFP-3D-Infinity atomic force microscopy (AFM).

**Electronic Transport and Magnetic Measurements:** The magnetic properties of the LCO films were measured using a Quantum Design Superconducting quantum interference device (SQUID) magnetometry measurements. The Magnetization–temperature ( $M$ – $T$ ) curves were measured at the magnetic field of 100 Oe applied along the films plane (in plane) after the field cooling in the same field. The in-plane magnetization-magnetic field hysteresis loops ( $M$ – $H$  curves) were measured at 10 K with magnetic field up to  $\pm 6$  T. DC transport measurements were carried out in a Quantum Design Physical Property Measurement System (PPMS) from 200 to 380 K under zero magnetic field.

**Soft X-Ray Spectroscopy Measurements:** X-ray spectroscopy measurements were carried out in the total electron yield mode (TEY) at the TLS11A and TPS45A beamline of the National Synchrotron Radiation Research Center (NSRRC) in Taiwan. The X-ray absorption spectroscopy (XAS) measurements were performed at 30 K temperature without applying magnetic field using TEY mode and an X-ray angle of incidence of 20° to the sample surface. X-ray linear dichroism (XLD) measurements were performed at 30 K and obtained from the difference of horizontal and vertical polarized light absorption spectra without applying magnetic field using TEY mode. The X-ray beam was incident on the sample at an angle of 20° from the sample surface. X-ray magnetic circular dichroism (XMCD) spectra were measured in the TEY mode without applying magnetic field using fixed X-ray circular polarization at 30 K in grazing incidence geometry. Before the XMCD measurement, the LCO films were first magnetized by a magnetic field of 1 Tesla.

**High-Resolution STEM Characterizations:** For cross-sectional microscopy, a sample was prepared by using focused ion beam (FIB) milling. Cross-sectional lamellas were thinned down to 60 nm thick at an accelerating voltage of 30 kV with a decreasing current from the maximum 2.5 nA, followed by fine polish at an accelerating voltage of 2 kV with a small current of 40 pA. The atomic scale HAADF-STEM images of LaCoO<sub>3</sub> films were performed by Cs-corrected JEM ARM200CF microscope operated at 200 kV using a high-angle annular detector for Z-contrast imaging; and the beam convergence angle was 28.5 mrad and a collection angle of 90–370 mrad.

**Configurational Cluster-Interaction (CI) Calculations:** This theoretical approach considers the fully atomic multiplet effect and configurational interaction as well as local solid effect. Three configurations, namely  $|3d^6\rangle$ ,  $|3d^7\bar{L}^1\rangle$ , and  $|3d^8\bar{L}^2\rangle$  were employed in the calculations, where  $|\bar{L}^n\rangle$  denotes the number of the holes on the ligand orbitals that make the bond with the  $\text{Co}^{3+}$  ion. These ligand orbitals were formed by the linear combination of oxygen 2p orbitals with respect to the local point symmetry of the  $\text{Co}^{3+}$  ion. The energy centers of each configuration are defined as  $|3d^6\rangle = 0$ ,  $|3d^7\bar{L}^1\rangle = \Delta$ , and  $|3d^8\bar{L}^2\rangle = 2\Delta + U_{dd}$ , where the charge transfer energy  $\Delta = 2.0$  eV and the Coulomb repulsion  $U_{dd} = 5.5$  eV were used in the calculations. The hybridization between these three configurations was determined by the parameter of  $\sqrt{3}pd\sigma$  that controlled the electron hopping between  $3d_{eg}$  and  $\bar{L}_{eg}$ , and the parameter of  $2pd\pi$ , which controlled the electron hopping between  $3d_{t2g}$  and  $\bar{L}_{t2g}$ .  $pd\sigma = 1.7$  eV and  $pd\pi = 0.74$  eV were taken for both high-spin and low-spin simulations. The electron–electron full-multiplet effect, which is a key determinant of the  $\text{Co}^{3+}$  spin state, was included in each configuration. The Slater integrals of  $F_2(dd) = 12.662(\text{eV})^*Slred$ ,  $F_4(dd) = 7.916(\text{eV})^*Slred$ , which were determined by the Hartree–Fock approximation using the R. D. Cowan code RCN36K, were used in the calculations to account for the atomic full-multiplet effect, where the parameters for Slater integral reductions ( $Slred = 0.75$ ) were further employed to compromise the solid-state effect.

In Figure S10a (Supporting Information) the total energy level diagram is plotted as a function of 10Dq. It can be seen that the ground state of the cluster is either low-spin (LS) or high-spin (HS) with a crossover at  $\approx 10Dq \approx 0.45$  eV. The 10Dq = 0.62 eV and 10Dq = 0.2 eV were chosen to calculate the LS and HS XAS, respectively. It is addressed that the reason of such low 10Dq that could achieve the HS–LS crossover was because of the presence of hybridization between  $\text{Co}^{3+}$  3d and oxygen ligand orbital, which effectively enhanced the splitting between  $e_g$  and  $t_{2g}$  level. In Figure S10b (Supporting Information), the total energy level diagram is plotted as a function of 10Dq under the single cluster calculation consid-



ering only  $3d^6$  configuration, that is, the hybridization between  $\text{Co}^{3+} 3d$  and oxygen ligand orbital is completely excluded. It could be seen that the HS–LS transition then increased to  $10\text{Dq} \approx 2.0$  eV.

To simulate LS and HS XAS, three configurations of  $|\underline{c}3d^7\rangle$ ,  $|\underline{c}3d^8\underline{L}^1\rangle$ , and  $|\underline{c}3d^9\underline{L}^2\rangle$  were employed, where  $\underline{c}$  denotes a hole that appeared in the Co  $2p$  core level after an electron transition to the  $3d$  orbital by X-ray. The energy centers of these three configurations are  $|\underline{c}3d^7\rangle = \epsilon_{\text{XAS}}$ ,  $|\underline{c}3d^8\underline{L}^1\rangle = \epsilon_{\text{XAS}} + \Delta + U_{\text{dd}} - U_{\text{dp}}$ , and  $|\underline{c}3d^9\underline{L}^2\rangle = \epsilon_{\text{XAS}} + 2\Delta + 3U_{\text{dd}} - 2U_{\text{dp}}$ , where the  $\epsilon_{\text{XAS}}$  is the energy required to excite an electron from the Co  $2p$  to the Co  $3d$  level. The  $U_{\text{dp}} = 7.0$  eV was used and the Slater integrals of  $F_2(\text{d-p}) = 7.899 \times \text{Slred}$ ,  $G_1(\text{d-p}) = 5.947 \times \text{Slred}$ , and  $G_3(\text{d-p}) = 3.384 \times \text{Slred}$  (with  $\text{Slred} = 0.75$ ) for the Co  $2p$ - $3d$  multiplet were further included in the calculation.

**First-Principle Calculations:** First-principles calculations were performed using the projector augmented wave method,<sup>[42]</sup> as implemented in the Vienna Ab initio Simulation Package (VASP).<sup>[43]</sup> The cutoff energy was 600 eV. The self-consistent convergence criterion was  $10^{-6}$  eV. The force convergence criterion was  $0.01$  eV  $\text{\AA}^{-1}$ . The pressure convergence threshold on the simulation cell was 1 kbar. The generalized gradient approximation was used with the Perdew–Burke–Ernzerhof parameterization (GGA-PBE) as the exchange–correlation functional.<sup>[44]</sup> A  $9 \times 9 \times 6$  Monkhorst–Pack grid<sup>[45]</sup> was used as the Brillouin zone integration. To model the correlation effects on Co  $3d$  orbitals, the rotationally invariant Hubbard  $U$  method was used.<sup>[46]</sup> Following the previous study,<sup>[47]</sup> it was found that a  $U_{\text{Co}} = 6$  eV reproduced the insulating properties of  $\text{LaCoO}_3$  thin films in both low-spin, high-spin, and mixed-spin states.  $U_{\text{La}} = 11$  eV was turned on for La- $4f$  orbitals so that they were moved away from the Fermi level. Bulk  $\text{LaCoO}_3$  had a crystal structure of space group  $R\bar{3}c$ . To simulate epitaxial strain, the previous study was followed and tetragonal conventional cell was adopted using the starting ionic positions as mapped from bulk  $\text{LaCoO}_3$ . The study defines  $a$  and  $b$  as the in-plane lattice parameters, whereas  $c$  is the out-of-plane lattice parameter. To simulate the epitaxial  $\text{LaCoO}_3$  thin films on different substrates, the in-plane lattice constant  $a = b = 5.57$   $\text{\AA}$  ( $\text{SrTiO}_3$ ) and  $a = b = 5.39$   $\text{\AA}$  ( $\text{LaAlO}_3$ ) were constrained, respectively. The out-of-plane lattice constant  $c$  and all the internal coordinates were fully relaxed. The conventional cell has four formula units (20 atoms). In the low-spin (LS) configuration, all the cobalt atoms were low-spin states. In the mix spin (MS) configuration, one of the cobalt was set to be in the high-spin state and the other three cobalt atoms were in the low-spin state.

The study shows the atomic projected density of states (PDOS) in Figure S3 (Supporting Information). Panel (a) is the PDOS of the  $\text{LaCoO}_3$  thin film under a  $\text{LaAlO}_3$  substrate (compressive strain). The calculations were done in a low-spin state, which yielded a gap of 1.63 eV. The conduction band edge was dominantly Co- $d$  states, while the valence band edge was mainly O- $p$  states that were strongly hybridized with Co- $d$  states. Panel (b) is the PDOS of the  $\text{LaCoO}_3$  thin film under a  $\text{SrTiO}_3$  substrate (tensile strain). Motivated by the experimental results, a mixed-spin state was calculated in which 75% Co atoms were in a low-spin state and the 25% Co atoms were in a high-spin state. It was found that the mixed-spin state was also insulating with a slightly smaller gap of 1.48 eV. The high-spin Co- $d$  state (red curve) had a strong splitting between spin-up and spin-down channel and yielded a magnetic moment of  $3.2\mu_{\text{B}}/\text{Co}$ . The splitting was roughly on the order of  $U_{\text{Co}} = 6$  eV. The low-spin Co- $d$  state (green curve) did not generate a net magnetization. The mixed-state had a net magnetization of  $1\mu_{\text{B}}$  per formula.

## Supporting Information

Supporting Information is available from the Wiley Online Library or from the author.

## Acknowledgements

This work was funded by the Guangdong Basic and Applied Basic Research Foundation (Grant No. 2020B1515020029), the Shenzhen Science

and Technology Innovation Project (Grant No. JCYJ20200109112829287), and the Shenzhen Science and Technology Program (Grant No. KQTD20200820113045083). Z.H.C. was supported by “the Fundamental Research Funds for the Central Universities” (Grant No. HIT.OCEF.2022038) and the “Talent Recruitment Project of Guangdong” (Grant No. 2019QN01C202). C.-Y.K. acknowledges the financial support from the Ministry of Science and Technology in Taiwan under grant no. MOST 110-2112-M-A49-002-MY3. C.F.C. and C.-Y.K. acknowledge support from the Max Planck-POSTECH-Hsinchu Center for Complex Phase Materials. Q.H.Z. acknowledges the financial support from National Natural Science Foundation of China (Grant Nos. 52072400 and 52025025) and Beijing Natural Science Foundation (Z190010). H.C. was financially supported by the National Key R&D Program of China under project number 2021YFE0107900.

## Conflict of Interest

The authors declare no conflict of interest.

## Data Availability Statement

The data that support the findings of this study are available from the corresponding author upon reasonable request.

## Keywords

epitaxial strain, insulating ferromagnetism,  $\text{LaCoO}_3$  thin films, spin state disproportionation, X-ray absorption spectroscopy

Received: June 3, 2023

Revised: June 30, 2023

Published online: July 23, 2023

- [1] N. Reyren, S. Thiel, A. D. Caviglia, L. F. Kourkoutis, G. Hammerl, C. Richter, C. W. Schneider, T. Kopp, A. S. Ruetschi, D. Jaccard, M. Gabay, D. A. Muller, J. M. Triscone, J. Mannhart, *Science* **2007**, 317, 1196.
- [2] J. H. Haeni, P. Irvin, W. Chang, R. Uecker, P. Reiche, Y. L. Li, S. Choudhury, W. Tian, M. E. Hawley, B. Craigo, A. K. Tagantsev, X. Q. Pan, S. K. Streiffer, L. Q. Chen, S. W. Kirchoefer, J. Levy, D. G. Schlom, *Nature* **2004**, 430, 758.
- [3] A. Brinkman, M. Huijben, M. Van Zalk, J. Huijben, U. Zeitler, J. C. Maan, W. G. Van der Wiel, G. Rijnders, D. H. A. Blank, H. Hilgenkamp, *Nat. Mater.* **2007**, 6, 493.
- [4] J. Wang, J. B. Neaton, H. Zheng, V. Nagarajan, S. B. Ogale, B. Liu, D. Viehland, V. Vaithyanathan, D. G. Schlom, U. V. Waghmare, N. A. Spaldin, K. M. Rabe, M. Wuttig, R. Ramesh, *Science* **2003**, 299, 1719.
- [5] Z. H. Chen, Z. H. Chen, Z. Q. Liu, M. E. Holtz, C. J. Li, X. R. Wang, W. M. Lu, M. Motapohtula, L. S. Fan, J. A. Turcaud, L. R. Dedon, C. Frederick, R. J. Xu, R. Gao, A. T. N'Diaye, E. Arenholz, J. A. Mundy, T. Venkatesan, D. A. Muller, L. W. Wang, J. Liu, L. W. Martin, *Phys. Rev. Lett.* **2017**, 119, 156801.
- [6] S. Chen, S. Yuan, Z. Hou, Y. Tang, J. Zhang, T. Wang, K. Li, W. Zhao, X. Liu, L. Chen, L. W. Martin, Z. Chen, *Adv. Mater.* **2021**, 33, 2000857.
- [7] J. H. Lee, L. Fang, E. Vlahos, X. L. Ke, Y. W. Jung, L. F. Kourkoutis, J. W. Kim, P. J. Ryan, T. Heeg, M. Roeckerath, V. Goian, M. Bernhagen, R. Uecker, P. C. Hammel, K. M. Rabe, S. Kamba, J. Schubert, J. W. Freeland, D. A. Muller, C. J. Fennie, P. Schiffer, V. Gopalan, E. Johnston-Halperin, D. G. Schlom, *Nature* **2010**, 466, 954.
- [8] D. Fuchs, C. Pinta, T. Schwarz, P. Schweiss, P. Nagel, S. Schuppler, R. Schneider, M. Merz, G. Roth, H. von Lohneysen, *Phys. Rev. B* **2007**, 75, 144402.



- [9] D. Fuchs, E. Arac, C. Pinta, S. Schuppler, R. Schneider, H. V. von Lohneysen, *Phys. Rev. B* **2008**, *77*, 014434.
- [10] M. W. Haverkort, Z. Hu, J. C. Cezar, T. Burnus, H. Hartmann, M. Reuther, C. Zobel, T. Lorenz, A. Tanaka, N. B. Brookes, H. H. Hsieh, H. J. Lin, C. T. Chen, L. H. Tjeng, *Phys. Rev. Lett.* **2006**, *97*, 176405.
- [11] M. J. R. Hoch, S. Nellutla, J. van Tol, E. S. Choi, J. Lu, H. Zheng, J. F. Mitchell, *Phys. Rev. B* **2009**, *79*, 214421.
- [12] M. Merz, P. Nagel, C. Pinta, A. Samartsev, H. von Lohneysen, M. Wissinger, S. Uebe, A. Assmann, D. Fuchs, S. Schuppler, *Phys. Rev. B* **2010**, *82*, 174416.
- [13] J. Fujioka, Y. Yamasaki, H. Nakao, R. Kumai, Y. Murakami, M. Nakamura, M. Kawasaki, Y. Tokura, *Phys. Rev. Lett.* **2013**, *111*, 027206.
- [14] N. Biskup, J. Salafranca, V. Mehta, M. P. Oxley, Y. Suzuki, S. J. Pennycook, S. T. Pantelides, M. Varela, *Phys. Rev. Lett.* **2014**, *112*, 087202.
- [15] V. V. Mehta, N. Biskup, C. Jenkins, E. Arenholz, M. Varela, Y. Suzuki, *Phys. Rev. B* **2015**, *91*, 144418.
- [16] Y. Yokoyama, Y. Yamasaki, M. Taguchi, Y. Hirata, K. Takubo, J. Miyawaki, Y. Harada, D. Asakura, J. Fujioka, M. Nakamura, H. Daimon, M. Kawasaki, Y. Tokura, H. Wadati, *Phys. Rev. Lett.* **2018**, *120*, 206402.
- [17] E. J. Guo, R. Desautels, D. Lee, M. A. Roldan, Z. L. Liao, T. Charlton, H. Ambaye, J. Molaison, R. Boehler, D. Keavney, A. Herklotz, T. Z. Ward, H. N. Lee, M. R. Fitzsimmons, *Phys. Rev. Lett.* **2019**, *122*, 187202.
- [18] J. Fujioka, Y. Yamasaki, A. Doi, H. Nakao, R. Kumai, Y. Murakami, M. Nakamura, M. Kawasaki, T. Arima, Y. Tokura, *Phys. Rev. B* **2015**, *92*, 195115.
- [19] H. Hsu, P. Blaha, R. M. Wentzcovitch, *Phys. Rev. B* **2012**, *85*, 140404.
- [20] K. Gupta, P. Mahadevan, *Phys. Rev. B* **2009**, *79*, 020406.
- [21] G. E. Sterbinsky, R. Nanguneri, J. X. Ma, J. Shi, E. Karapetrova, J. C. Woicik, H. Park, J. W. Kim, P. J. Ryan, *Phys. Rev. Lett.* **2018**, *120*, 197201.
- [22] W. S. Choi, J. H. Kwon, H. Jeon, J. E. Hamann-Borrero, A. Radi, S. Macke, R. Sutarto, F. Z. He, G. A. Sawatzky, V. Hinkov, M. Kim, H. N. Lee, *Nano Lett.* **2012**, *12*, 4966.
- [23] S. Yoon, X. Gao, J. M. Ok, Z. L. Liao, M. G. Han, Y. M. Zhu, P. Ganesh, M. F. Chisholm, W. S. Choi, H. N. Lee, *Nano Lett.* **2021**, *21*, 4006.
- [24] T. Huang, Y. Lyu, H. Huyan, J. Ni, S. Saremi, Y. Wang, X. Yan, D. Yi, Q. He, L. W. Martin, H. Xiang, X. Pan, P. Yu, *Adv. Electron. Mater.* **2023**, *9*, 2201245.
- [25] J. W. Freeland, J. X. Ma, J. Shi, *Appl. Phys. Lett.* **2008**, *93*, 212501.
- [26] D. C. Meng, H. L. Guo, Z. Z. Cui, C. Ma, J. Zhao, J. B. Lu, H. Xu, Z. C. Wang, X. Hu, Z. P. Fu, R. R. Peng, J. H. Guo, X. F. Zhai, G. J. Brown, R. Knize, Y. L. Lu, *Proc. Natl. Acad. Sci. USA* **2018**, *115*, 2873.
- [27] V. Chaturvedi, J. Walter, A. Paul, A. Grutter, B. Kirby, J. S. Jeong, H. Zhou, Z. Zhang, B. Q. Yu, M. Greven, K. A. Mkhoyan, T. Birol, C. Leighton, *Phys. Rev. Mater.* **2020**, *4*, 034403.
- [28] Z. Hu, H. Wu, M. W. Haverkort, H. H. Hsieh, H. J. Lin, T. Lorenz, J. Baier, A. Reichl, I. Bonn, C. Felser, A. Tanaka, C. T. Chen, L. H. Tjeng, *Phys. Rev. Lett.* **2004**, *92*, 207402.
- [29] T. Burnus, Z. Hu, M. W. Haverkort, J. C. Cezar, D. Flahaut, V. Hardy, A. Maignan, N. B. Brookes, A. Tanaka, H.-H. Hsieh, *Phys. Rev. B* **2006**, *74*, 245111.
- [30] Y. Y. Chin, Z. Hu, Y. Su, Y. Tsujimoto, A. Tanaka, C. T. Chen, *Phys. Status Solidi Rapid Res. Lett.* **2018**, *12*, 1800147.
- [31] Q. Y. Feng, D. C. Meng, H. B. Zhou, G. H. Liang, Z. Z. Cui, H. L. Huang, J. L. Wang, J. H. Guo, C. Ma, X. F. Zhai, Q. Y. Lu, Y. L. Lu, *Phys. Rev. Mater.* **2019**, *3*, 074406.
- [32] J. H. Kwon, W. S. Choi, Y. K. Kwon, R. Jung, J. M. Zuo, H. N. Lee, M. Kim, *Chem. Mater.* **2014**, *26*, 2496.
- [33] Q. Q. Lan, X. Shen, H. W. Yang, H. R. Zhang, J. Zhang, X. X. Guan, Y. Yao, Y. G. Wang, R. C. Yu, Y. Peng, J. R. Sun, *Appl. Phys. Lett.* **2015**, *107*, 242404.
- [34] H. Zhang, J. Zhang, H. Yang, Q. Lan, D. Hong, S. Wang, X. Shen, T. Khan, R. Yu, J. Sun, B. Shen, *ACS Appl. Mater. Interfaces* **2016**, *8*, 18328.
- [35] J. H. Jang, Y. M. Kim, Q. He, R. Mishra, L. Qiao, M. D. Biegalski, A. R. Lupini, S. T. Pantelides, S. J. Pennycook, S. V. Kalinin, A. Y. Borisevich, *ACS Nano* **2017**, *11*, 6942.
- [36] J. Badro, G. Fiquet, V. V. Struzhkin, M. Somayazulu, H.-k. Mao, G. Shen, T. Le Bihan, *Phys. Rev. Lett.* **2002**, *89*, 205504.
- [37] J. Kuneš, D. M. Korotin, M. Korotin, V. Anisimov, P. Werner, *Phys. Rev. Lett.* **2009**, *102*, 146402.
- [38] D. Wu, G.-d. Chen, C.-y. Ge, Z.-p. Hu, X.-h. He, X.-g. Li, *Chin. J. Chem. Phys.* **2017**, *30*, 295.
- [39] W. T. Hong, M. Gadre, Y. L. Lee, M. D. Biegalski, H. M. Christen, D. Morgan, Y. Shao-Horn, *J. Phys. Chem. Lett.* **2013**, *4*, 2493.
- [40] J. Kuneš, V. Křápek, *Phys. Rev. Lett.* **2011**, *106*, 256401.
- [41] G. E. Sterbinsky, P. J. Ryan, J. W. Kim, E. Karapetrova, J. X. Ma, J. Shi, J. C. Woicik, *Phys. Rev. B* **2012**, *85*, 020403.
- [42] G. Kresse, J. Furthmüller, *Phys. Rev. B* **1996**, *54*, 11169.
- [43] G. Kresse, J. Hafner, *Phys. Rev. B* **1994**, *49*, 14251.
- [44] J. P. Perdew, K. Burke, M. Ernzerhof, *Phys. Rev. Lett.* **1996**, *77*, 3865.
- [45] H. J. Monkhorst, J. D. Pack, *Phys. Rev. B* **1976**, *13*, 5188.
- [46] S. L. Dudarev, G. A. Botton, S. Y. Savrasov, C. J. Humphreys, A. P. Sutton, *Phys. Rev. B* **1998**, *57*, 1505.
- [47] K. Saritas, J. T. Krogel, S. Okamoto, H. N. Lee, F. A. Reboredo, *Phys. Rev. Mater.* **2019**, *3*, 124414.